J|A|C|S ARTICLES

Published on Web 11/02/2009

Tomographic Energy Dispersive Diffraction Imaging To Study the Genesis of Ni Nanoparticles in 3D within γ-Al_2O_3 Catalyst Bodies

Leticia Espinosa-Alonso,[†] Matthew G. O'Brien,[†] Simon D. M. Jacques,[‡,§] Andrew M. Beale,[†] Krijn P. de Jong,[†] Paul Barnes,[‡,§] and Bert M. Weckhuysen*[,†]

Inorganic Chemistry and Catalysis, Debye Institute for Nanomaterials Science, Utrecht University, Sorbonnelaan 16, 3584 CA Utrecht, The Netherlands, Department of Chemistry, University College London, 20 Gordon Street, London WC1H 0AJ, United Kingdom, and Industrial Materials Group, Department of Crystallography, Birkbeck College, Malet Street, London WC1E 7HX, United Kingdom

Received August 30, 2009; E-mail: b.m.weckhuysen@uu.nl

Abstract: Tomographic energy dispersive diffraction imaging (TEDDI) is a recently developed synchrotron-based characterization technique used to obtain spatially resolved X-ray diffraction and fluorescence information in a noninvasive manner. With the use of a synchrotron beam, three-dimensional (3D) information can be conveniently obtained on the elemental composition and related crystalline phases of the interior of a material. In this work, we show for the first time its application to characterize the structure of a heterogeneous catalyst body in situ during thermal treatment. Ni/γ-Al_2O_3 hydrogenation catalyst bodies have been chosen as the system of study. As a first example, the heat treatment in N_2 of a $[Ni(en)_3](NO_3)_2$/γ-Al_2O_3 catalyst body has been studied. In this case, the crystalline $[Ni(en)_3](NO_3)_2$ precursor was detected in an egg-shell distribution, and its decomposition to form metallic Ni crystallites of around 5 nm was imaged. In the second example, the heat treatment in N_2 of a $[Ni(en)(H_2O)_4]Cl_2$/γ-Al_2O_3 catalyst body was followed. The initial $[Ni(en)(H_2O)_4]Cl_2$ precursor was uniformly distributed within the catalyst body as an amorphous material and was decomposed to form metallic Ni crystallites of around 30 nm with a uniform distribution. TEDDI also revealed that the decomposition of $[Ni(en)(H_2O)_4]Cl_2$ takes place via two intermediate crystalline structures. The first one, which appears at around 180 °C, is related to the restructuring of the Ni precursor on the alumina surface; the second one, assigned to the formation of a limited amount of Ni_3C, is observed at 290 °C.

Introduction

For many industrial applications, heterogeneous catalysts in the form of preshaped catalyst bodies with sizes in the range of a few millimeters to a few tenths of micrometers are required.[1,2] These catalyst bodies consist of a preshaped support such as γ-Al_2O_3 and an active component, usually a metal, metal oxide, or metal sulfide, depending on the chemical reaction for which the catalyst is used. Supported catalysts are generally prepared via pore volume impregnation of a solution containing the precursor of the active species followed by drying, calcination, and, if required, other activation treatments such as reduction or sulfidation.[3,4] The preparation procedure determines the nature of the active phase and its macrodistribution within the catalyst body.[5] In general, four different macrodistributions (uniform, egg-shell, egg-yolk, or egg-white) can be obtained, and each of these has specific industrial applications.[6] For this reason, the catalyst preparation procedure is of prime importance since it determines the efficiency and the lifetime of the catalyst. As a consequence, improved control in the nature and distribution of the active component during the different catalyst preparation steps is of utmost interest for the industrial community.

To achieve this goal, new spectroscopic techniques with improved spatiotemporal resolution are being developed and applied.[7] Nowadays, the goal of the catalyst scientist is to utilize techniques that provide three-dimensional (3D) information of the real structure of the catalyst body during its preparation. In this regard, several methods have already been developed that provide spatial information on the nature of the active species and its transport within the support body during the impregnation step, after drying or calcination, namely, UV−vis, Raman, and IR microspectroscopies. These three are one-dimensional (1D)

[†] Utrecht University.
[‡] University College London.
[§] Birkbeck College.

(1) *Preparation of Solid Catalysts*; Ertl, G., Knozinger, H., Weitkamp, J., Eds.; Wiley-VHC: Weinheim, Germany, 1999.
(2) *Catalyst Preparation: Science and Engineering*; Regalbuto, J. R., Ed.; CRC Press: Boca Raton, FL, 2007.
(3) *Synthesis of Solid Catalysts*; de Jong, K. P., Ed.; Wiley-VCH: Weinheim, Germany, 2009.
(4) Sietsma, J. R. A.; Meeldijk, J. D.; Versluijs-Helder, M.; Broersma, A.; van Dillen, A. J.; de Jongh, P. E.; de Jong, K. P. *Chem. Mater.* **2008**, *20*, 2921–2931.
(5) Sietsma, J. R. A.; Meeldijk, J. D.; den Breejen, J. P.; Versluijs-Helder, M.; van Dillen, A. J.; de Jongh, P. E.; de Jong, K. P. *Angew. Chem., Int. Ed.* **2007**, *46*, 4547–4549.
(6) Neimark, A. V.; Kheifets, L. I.; Fenelonov, V. B. *Ind. Eng. Chem. Prod. Res. Dev.* **1981**, *20*, 439–450.
(7) Weckhuysen, B. M. *Angew. Chem., Int. Ed.* **2009**, *48*, 4910–4943.

10.1021/ja907329j CCC: $40.75

techniques that provide chemical information along a scan-line of the catalyst body.[8−10] Consequently, it has to be assumed that the obtained information is representative for the whole volume of the sample under study. Moreover, to apply these techniques, a prebisection of the sample is required. Therefore, with the exception of the study of the impregnation step that only requires a wet atmosphere around the sample, these techniques cannot be used during in situ preparation conditions and hence the need for the development and application of noninvasive techniques. Magnetic resonance imaging (MRI) lies in this group of techniques, and it has been successfully used to monitor the mobility of paramagnetic metal complexes during impregnation of catalyst bodies in a two-dimensional (2D) manner.[11−14] Moreover, it has been used under reaction conditions to monitor temperature gradients inside a catalytic reactor and to monitor the reactant liquid inside a catalyst pellet.[15,16] More recently, the potential of synchrotron radiation has been explored to obtain further insight in this field. Tomographic energy dispersive diffraction imaging (TEDDI) and X-ray microtomography are such types of synchrotron-based techniques which provide spatial information in 3D. While the latter yields information on the pore structure of the support body, the former provides crystalline phase distribution maps as well as information on the elemental distributions of the active component from the available fluorescence signals.[17−24]

In this work, we show for the first time the application of TEDDI under realistic preparation conditions, that is, during heat treatment, often referred to as the calcination step, of a heterogeneous catalyst. The aim was to obtain insight into the changes in the molecular structure of the precursor metal−ion complex along the catalyst body as a function of temperature. For this purpose, the calcination of Ni/γ-Al_2O_3 hydrogenation catalyst bodies has been chosen as the system to investigate, and two examples with different precursor complexes containing ethylenediamine (en) have been studied, namely, $[Ni(en)(H_2O)_4]Cl_2$ and $[Ni(en)_3](NO_3)_2$. These precursors are known to yield, under specific experimental conditions such as calcination under an inert atmosphere, highly dispersed metallic Ni particles on powdered catalysts.[25−31] TEDDI has been used here for the chemical imaging of the genesis of Ni nanoparticles in 3D within γ-Al_2O_3 catalyst bodies.

Materials and Methods

Materials. The support material used on this study was γ-Al_2O_3 in the form of pellets (Engelhard, 3 mm length and diameter). The pore volume was 0.7 mL/g, the surface area was 209 m^2/g, and the pore size was 13 nm as determined by N_2-physisorption. The point of zero charge (pzc) was determined to be 7.8 by mass titration.[32]

Two different catalytic materials were prepared from the precursor complexes $[Ni(en)_3](NO_3)_2$ and $[Ni(en)(H_2O)_4]Cl_2$ (en, ethylenediamine). The final metallic Ni content was 10 wt %, and the samples differed with respect to the Ni precursor salt (nitrate or chloride) and in the molar en:Ni ratio.

The nitrate sample, $[Ni(en)_3](NO_3)_2/\gamma$-$Al_2O_3$, was prepared via pore volume impregnation of a solution containing 1.9 M $Ni(NO_3)_2 \cdot 6H_2O$ (Acros, p.a.) and 5.7 M ethylenediamine (en, Acros, p.a.) of the γ-Al_2O_3 pellets. As the impregnation solution was not stable at 25 °C and crystallized after a short time forming $[Ni(en)_3](NO_3)_2$ crystals, it was warmed up to 60 °C for 30 min prior to impregnation. Pore volume impregnation was then carried out as follows: a 0.9 g batch of γ-Al_2O_3 pellets and a syringe containing the required volume of the impregnation solution were kept at 60 °C for 4 h. After that time, the pellets were impregnated dropwise in 2 min and were shaken manually for 2 min to ensure a homogeneous distribution of the solution on the pellets. Subsequently, the pellets were left to equilibrate in a closed vessel for 2 h in an oven at 60 °C to avoid crystallization of $[Ni(en)_3](NO_3)_2$. The vessel contained a wet tissue on top to avoid drying of the pellets. After that time, the pellets were dried at 20 °C (room temperature) overnight.

The chloride sample, $[Ni(en)(H_2O)_4]Cl_2/\gamma$-$Al_2O_3$, was prepared via pore volume impregnation of a solution containing 1.9 M $NiCl_2 \cdot 6H_2O$ (Acros, p.a.) and 1.9 M ethylenediamine (en, Acros, p.a.) on the γ-Al_2O_3 pellets. The solution was stable at 20 °C, and pore volume impregnation was performed at 20 °C by adding the solution dropwise on the pellets. The addition was followed by manual shaking for 2 min, and the pellets were subsequently equilibrated for 2 h in a closed vessel with a wet tissue to avoid drying. The pellets were then dried at 20 °C overnight.

In Situ Calcination Experiments. Calcination of a single catalyst body of the prepared samples was carried out by heating from 25 to 500 °C (4 °C/min) under a flowing N_2 environment. This controlled atmosphere was realized using an environmental cell specifically designed to provide an oxygen-free environment while performing the TEDDI experiments (Figure S7 in the Supporting Information). The cell is schematically depicted in Figure 1.

(8) Bergwerff, J. A.; Visser, T.; Leliveld, G.; Rossenaar, B. D.; de Jong, K. P.; Weckhuysen, B. M. *J. Am. Chem. Soc.* **2004**, *126*, 14548–14556.
(9) Espinosa-Alonso, L.; de Jong, K. P.; Weckhuysen, B. M. *J. Phys. Chem. C* **2008**, *112*, 7201–7209.
(10) van de Water, L. G. A.; Bezemer, G. L.; Bergwerff, J. A.; Versluijs-Helder, M.; Weckhuysen, B. M.; de Jong, K. P. *J. Catal.* **2006**, *242*, 287–298.
(11) Bergwerff, J. A.; Lysova, A. A.; Espinosa Alonso, L.; Koptyug, I. V.; Weckhuysen, B. M. *Angew. Chem., Int. Ed.* **2007**, *46*, 7224–7227.
(12) Bergwerff, J. A.; Lysova, A. A.; Espinosa-Alonso, L.; Koptyug, I. V.; Weckhuysen, B. M. *Chem.—Eur. J.* **2008**, *14*, 2363–2374.
(13) Espinosa-Alonso, L.; Lysova, A. A.; de Peinder, P.; de Jong, K. P.; Koptyug, I. V.; Weckhuysen, B. M. *J. Am. Chem. Soc.* **2009**, *131*, 6525–6534.
(14) Lysova, A. A.; Koptyug, I. V.; Sagdeev, R. Z.; Parmon, V. N.; Bergwerff, J. A.; Weckhuysen, B. M. *J. Am. Chem. Soc.* **2005**, *127*, 11916–11917.
(15) Koptyug, I. V.; Khomichev, A. V.; Lysova, A. A.; Sagdeev, R. Z. *J. Am. Chem. Soc.* **2008**, *130*, 10452–10453.
(16) Koptyug, I. V.; Kulikov, A. V.; Lysova, A. A.; Kirillov, V. A.; Parmon, V. N.; Sagdeev, R. Z. *J. Am. Chem. Soc.* **2002**, *124*, 9684–9685.
(17) Beale, A. M.; Jacques, S. D. M.; Bergwerff, J. A.; Barnes, P.; Weckhuysen, B. M. *Angew. Chem., Int. Ed.* **2007**, *46*, 8832–8835.
(18) Bleuet, P.; Welcomme, E.; Dooryhee, E.; Susini, J.; Hodeau, J.-L.; Walter, P. *Nat. Mater.* **2008**, *7*, 468–472.
(19) Grunwaldt, J.-D.; Kimmerle, B.; Baiker, A.; Boye, P.; Schroer, C. G.; Glatzel, P.; Borca, C. N.; Beckmann, F. *Catal. Today* **2009**, *145*, 267–278.
(20) Hall, C.; Colston, S. L.; Jupe, A. C.; Jacques, S. D. M.; Livingston, R.; Ramadan, A. O. A.; Amde, A. W.; Barnes, P. *Cem. Concr. Res.* **2000**, *30*, 491–495.
(21) Jacques, S. D. M.; Pile, K.; Barnes, P.; Lai, X.; Roberts, K. J.; Williams, R. A. *Cryst. Growth Des.* **2005**, *5*, 395–397.
(22) Jonesa, K. W.; Fengb, H.; Lanzirottic, A.; Mahajan, D. *Top. Catal.* **2005**, *32*, 263–272.
(23) King, A.; Johnson, G.; Engelberg, D.; Ludwig, W.; Marrow, J. *Science* **2008**, *321*, 382–385.
(24) Ruffino, L.; Mann, R.; Oldman, R.; Stitt, E. H.; Boller, E.; Cloetens, P.; DiMichiel, M.; Merino, J. *Can. J. Chem. Eng.* **2005**, *83*, 132–139.
(25) Lambert, J.-F.; Hoogland, M.; Che, M. *J. Phys. Chem. B* **1997**, *101*, 10347–10355.
(26) Negrier, F.; Marceau, E.; Che, M. *Chem. Commun.* **2002**, 1194–1195.
(27) Negrier, F.; Marceau, E.; Che, M.; de Caro, D. *C. R. Chim.* **2003**, *6*, 231–240.
(28) Negrier, F.; Marceau, E.; Che, M.; Giraudon, J. M.; Gengembre, L.; Lofberg, A. *J. Phys. Chem. B* **2005**, *109*, 2836–2845.
(29) Négrier, F.; Marceau, E.; Che, M.; Giraudon, J.-M.; Gengembre, L.; Löfberg, A. *Catal. Lett.* **2008**, *124*, 18–23.
(30) Schimpf, S.; Louis, C.; Claus, P. *Appl. Catal., A: Gen.* **2007**, *318*, 45–53.
(31) Sun, K.-Q.; Marceau, E.; Che, M. *Phys. Chem. Chem. Phys.* **2006**, *8*, 1731–1738.
(32) Park, J.; Regalbuto, J. R. *J. Colloid Interface Sci.* **1995**, *175*, 239–252.

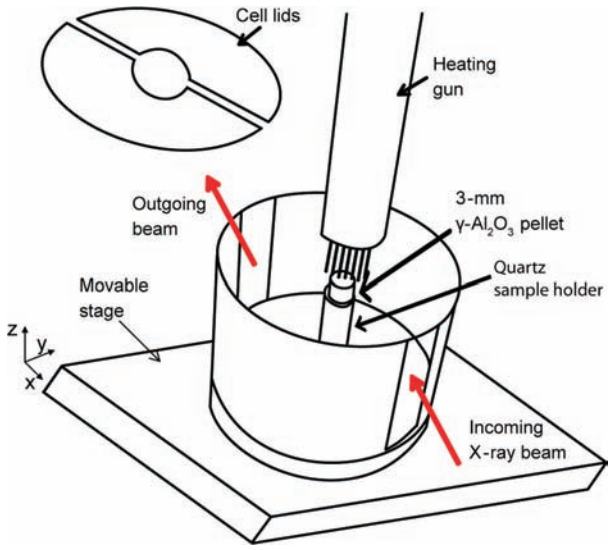

Figure 1. Schematic of the environmental cell designed for in situ calcination TEDDI experiments.

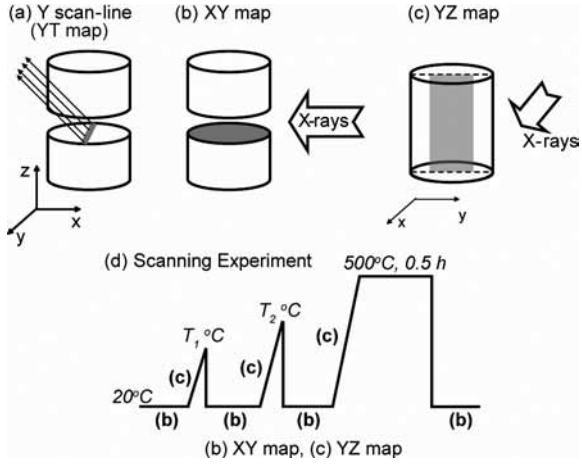

Figure 2. Scanning experiments performed (a−c) during calcination (d): (a) 1D Y scan-line with temperature (YT map), (b) 2D XY map, and (c) 2D YZ map. The gray areas represent the scanning regions during the calcination process. To collect the XY maps, the samples were quenched according to the temperature profiles depicted in d.

The environmental cell consisted of a stainless steel cylinder (9.5 cm height and 10.5 cm diameter) located on a movable (x, y, z) stage as depicted in Figure 1. The cylinder consisted of a quartz sample holder upon which the catalyst body was mounted. A heating gun located 1 cm above the pellet provided the N_2 at a controlled temperature and flow. The cell contained two Kapton windows (0.25 mm thickness) through which the incident X-ray beam enters and the scattered/emitted signal leaves. Finally, the integrity of the environmental cell was maintained at the top with two removable stainless steel lids. Scanning of the catalyst body inside the environmental cell was then performed in a stepwise manner in the x, y, and z directions as indicated in Figure 1. The scanning volume in each position of the catalyst body was determined to be $2.47 \times 0.1 \times 0.2$ mm^3 ($x \times y \times z$). More details can be found in the Supporting Information.

TEDDI Measurements. Three different scanning experiments were conducted, and a schematic of these with regard to the catalyst body is depicted in Figure 2. First, a Y scan-line in the center of the catalyst body (1D scan where $x = z = 0$ mm = center of the pellet) was measured continuously on a pellet during the calcination and will be referred to as YT map as depicted in Figure 2a. The step size was 0.2 mm and the time needed to measure one scan-line was 5.5 min. Second, a high-quality XY map (2D scan with $z = 0$ mm) was acquired on a new pellet at several temperatures during the calcination process (Figure 2b). The step size was 0.2 mm in the x and y directions, and the time required to obtain one XY map was 3.7 h. As illustrated in Figure 2d, because of the long scanning times of the XY maps, to relate these maps to specific temperature points in the calcination process, the samples were quenched to 25 °C after calcination for acquisition of the XY maps. Previous experiments have demonstrated that this quenching did not cause significant differences in the final Ni phase. Finally, YZ maps were collected (2D scans with $x = 0$ mm) in situ during the calcination; thus, between 25 °C and the selected temperature to measure an XY map; see Figure 2c and 2d. The step size was 1.3 mm in the x direction and 0.2 mm in the z direction; 6.8 min was required to collect a YZ map.

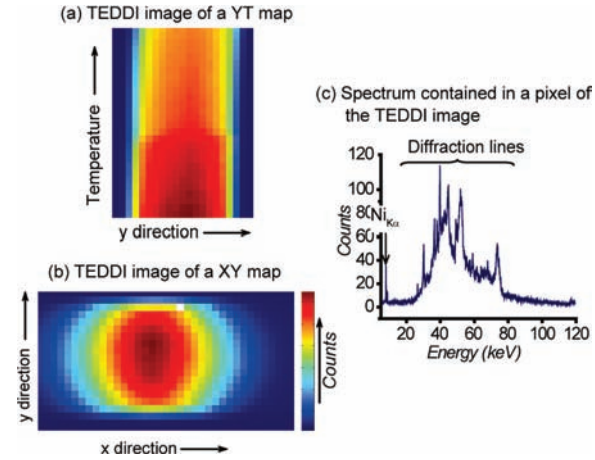

Figure 3. Raw TEDDI images of (a) a YT map and (b) an XY map on the pellet after the selected temperature and quenching and (c) typical total spectrum contained in a pixel of a TEDDI image. The blue pixels represent spectra with a low number of total counts, and the red pixels represent regions with a high number of counts.

Figure 3 shows the typical raw TEDDI images obtained from a YT and an XY map of a catalyst body.

Each pixel in the TEDDI images pertains to an associated energy-dispersive spectrum, as illustrated in Figure 3c, and a scanning volume of $2.47 \times 0.1 \times 0.2$ mm^3 ($x \times y \times z$). Such a spectrum contains two types of information, namely, the fluorescence signal from the Ni ($Ni_{K\alpha}$ at 7.5 keV) and the Bragg reflections from the crystalline catalytic material, that is, the γ-Al_2O_3 support body and other Ni crystalline phases. Concentration maps related to the appropriate diffraction or fluorescence peaks can be constructed of selected phases on the basis of the area (or intensity) of the fitted peaks above the background level. Batch multiple data processing of the TEDDI images were performed using the EasyEDD software developed by Lazzari et al.[33]

The XY maps of the pellet appear slightly elongated (i.e., not truly circular) in the x direction because of the asymmetric shape of the scanning volume with a significantly longer x-dimension (2.47 mm). Moreover, low energy peaks, such as Ni-fluorescence lines, will suffer more noticeably from attenuation through X-ray absorption depending on the paths that the X-rays take through the sample to each pixel in question and out until reaching the detector. It is difficult to accurately correct for this effect with samples containing material density and X-ray absorption coefficients that vary with spatial position and with time. However, a simple first-level correction can be made to improve the fluorescence distribution information that only takes into account the scanning volume and the distance that the X-rays had to travel to reach the detector, while self-reabsorption by Ni is ignored. Further details regarding the

(33) Lazzari, O.; Jacques, S.; Sochi, T.; Barnes, P. *Analyst* **2009**, *134*, 1802–1807.

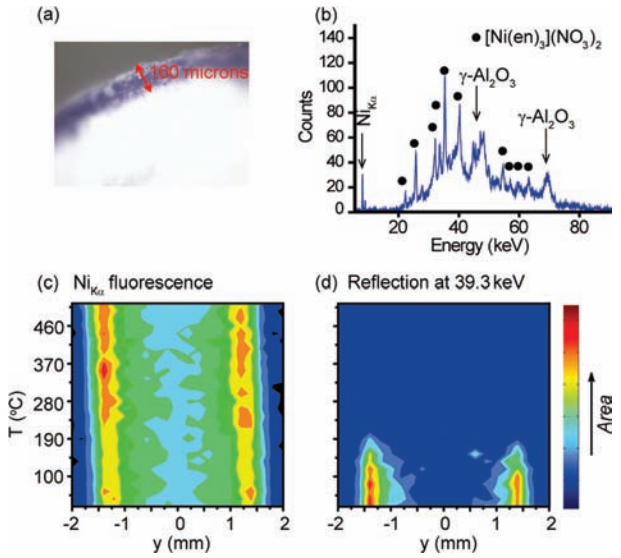

Figure 4. (a) Optical micrograph of the dried and bisected $[Ni(en)_3](NO_3)_2/\gamma\text{-}Al_2O_3$ pellet. (b) Energy-dispersive spectrum collected by TEDDI from the edge of the pellet before calcination. The $Ni_{K\alpha}$ fluorescence signal is indicated together with the diffraction peaks of the $[Ni(en)_3](NO_3)_2$ crystals and of $\gamma\text{-}Al_2O_3$. (c, d) YT maps in the $[Ni(en)_3](NO_3)_2/\gamma\text{-}Al_2O_3$ pellet for (c) the $Ni_{K\alpha}$ fluorescence and (d) the diffraction peak at 39.3 keV of the $[Ni(en)_3](NO_3)_2$ crystalline phase. The $y = 0$ point corresponds to the center of the pellet.

corrections applied to construct the 2D Ni-fluorescence maps can be found in the Supporting Information.

Results and Discussion

1. TEDDI during the Calcination of the $[Ni(en)_3](NO_3)_2/\gamma\text{-}Al_2O_3$ Pellet. Figure 4a shows an optical micrograph of a bisected $[Ni(en)_3](NO_3)_2/\gamma\text{-}Al_2O_3$ pellet after drying. A crust of 160 μm $[Ni(en)_3](NO_3)_2$ crystallites is clearly seen close to the edges of the catalyst body (egg-shell distribution of Ni). These crystallites formed during drying with the nucleation points probably being the pore mouths on the outer surface of the catalyst body. Figure 4b shows the energy-dispersive spectrum near the edges of the catalyst body prior to calcination. This spectrum contains several peaks between 20 and 68 keV in addition to the expected $Ni_{K\alpha}$ fluorescence line. By comparison with a high-quality angular-dispersive pattern (standard lab-based X-ray diffraction (XRD) pattern) of unsupported $[Ni(en)_3](NO_3)_2$ crystals (Supporting Information Figure S8a), it was possible to assign the peaks at 26.1, 29.6, 36.2, 37.5, 39.3, 44.2, 58.6, 61.0, 63.4, and 67.2 keV to the $[Ni(en)_3](NO_3)_2$ phase.[29] In addition, two peaks due to the $\gamma\text{-}Al_2O_3$ support were identified at 51.9 and 73.1 keV, which corresponded to the reflections (400) and (440).[34]

The YT maps in Figure 4c and 4d illustrate the distribution of Ni (amorphous and crystalline) and of crystalline $[Ni(en)_3](NO_3)_2$ with calcination temperature, respectively. From these maps, an initial Ni egg-shell distribution was deduced corresponding with the optically observed distribution in Figure 4a. The fluorescence map indicates that Ni, regardless of its crystalline structure, was mainly concentrated at the edges of the pellet, although some was present in the core. However, as the map of the crystalline $[Ni(en)_3](NO_3)_2$ indicated a sharp egg-shell profile of about 200 μm (cf. 160 μm observed optically), we can conclude that the core Ni was amorphous in structure.

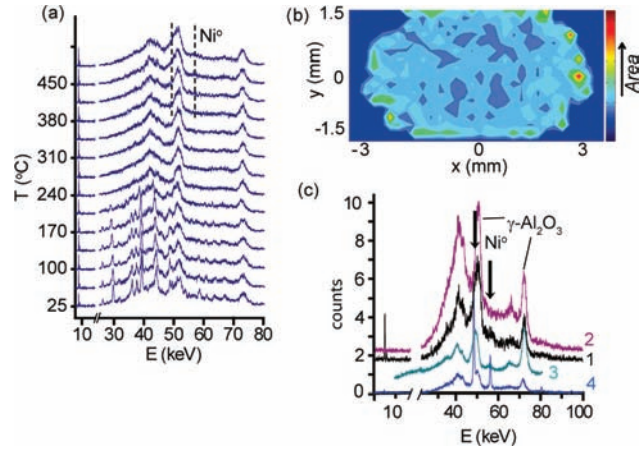

Figure 5. (a) Energy-dispersive spectra collected at the edge of the $[Ni(en)_3](NO_3)_2/\gamma\text{-}Al_2O_3$ pellet during the YT scanning experiment. The weak diffraction peaks of metallic Ni are marked with dashed lines. The spectra at low temperatures (<190 °C) also show the diffraction peaks of the $[Ni(en)_3](NO_3)_2$ precursor salt. (b) XY concentration map of metallic Ni after calcination constructed from the (200) reflection. (c) Spectrum at 500 °C at the edge of the $[Ni(en)_3](NO_3)_2/\gamma\text{-}Al_2O_3$ pellet (1) together with other reference spectra: $\gamma\text{-}Al_2O_3$ (2), XRD on the crushed $[Ni(en)_3](NO_3)_2/\gamma\text{-}Al_2O_3$ pellet after calcination at 500 °C (3), and large particles of Ni° on $\gamma\text{-}Al_2O_3$ ($[Ni(en)(H_2O)_4]Cl_2/\gamma\text{-}Al_2O_3$ pellet) (4).

Moreover, the $[Ni(en)_3](NO_3)_2$ crystals disappeared rapidly when the sample was heated above 190 °C indicating its decomposition to primarily an amorphous state. Still, by using the fluorescence data, it was determined that the Ni remained at the edges of the pellet and did not migrate toward the core.

Furthermore, a detailed examination of the energy-dispersive spectra indicated the presence of very small metallic Ni particles forming at higher temperatures. As an example, the spectra measured at the edge of the pellet during the calcination are given in Figure 5a. In them, a very weak diffraction peak appears at 57.6 keV at around 400 °C together with a shoulder on the low energy side (49.8 keV) of the Al_2O_3 diffraction peak at 51.9 keV. These two peaks, at 49.8 and 57.6 keV, are consistent with the (111) and (200) reflections of fcc (face-centered cubic) Ni.[35] From the TEDDI experiments, it cannot be deduced which fraction of the Ni species is present as metallic nanoparticles. From literature, we estimate that approximately 20% of the Ni was present as metallic nanoparticles.[29] Hence, 80% of the initial Ni species are forming other structures which are amorphous in nature since no other diffraction lines besides the ones from metallic nickel were observed. It is possible that part of the Ni species is forming the common nickel aluminate phase that is created when Ni/Al_2O_3 catalysts are prepared from the nitrate precursor. For comparison purposes, Figure 5c shows the energy-dispersive spectrum at the edge of the pellet at 500 °C (1) together with other reference spectra: an energy-dispersive spectrum somewhere on a $\gamma\text{-}Al_2O_3$ pellet without impregnation (the peak at 57.6 keV is not observed), the XRD pattern (in energy units) of a crushed postcalcined pellet which also contains a small peak at 57.6 keV, and the energy-dispersive spectrum at the edge of a sample which contains large metallic Ni particles and $\gamma\text{-}Al_2O_3$.

Figure 5b shows the XY map of the metallic Ni distribution after calcination at 500 °C derived from the fit of the (200) reflection and indicates that the metal is also present in an egg-shell distribution. From a Debye−Scherrer analysis on the

(34) Gutiérrez, G.; Taga, A.; Johansson, B. *Phys. Rev. B* **2001**, *65*, 012101.

(35) Owen, E. A.; Yates, E. L. *Philos. Mag.* **1936**, 809–819.

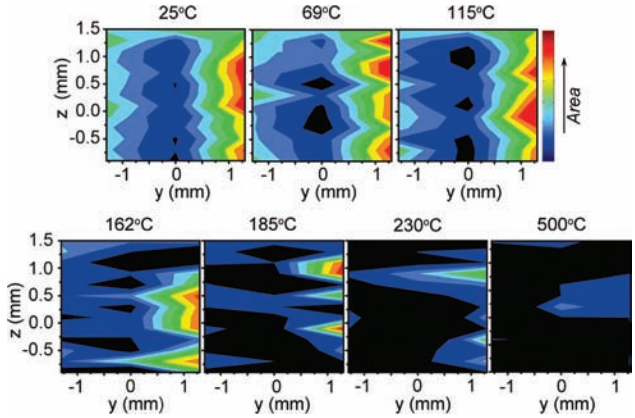

Figure 6. YZ maps of the $Ni(en)_3(NO_3)_2$ diffraction peak at 39.3 keV during the calcination process of the dried $[Ni(en)_3](NO_3)_2/\gamma$-$Al_2O_3$ pellet. The black regions indicate the absence of this peak while the red regions indicate high concentrations.

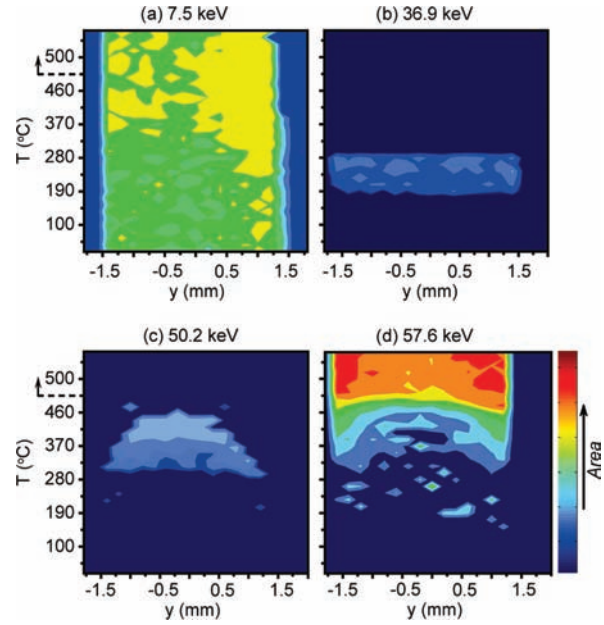

Figure 7. YT maps of (a) Ni fluorescence at 7.5 keV ($Ni_{K\alpha}$), (b) the diffraction peak at 36.9 keV (unknown Ni-containing crystalline phase), (c) the 50.2 keV (101) reflection of Ni_3C, and (d) the 57.6 keV (200) reflection of metallic fcc Ni, all in the $[Ni(en)(H_2O)_4]Cl_2/\gamma$-$Al_2O_3$ pellet. The red color represents regions where the concentration of the corresponding Ni species is the highest.

crushed postcalcined pellet (standard XRD), the size of these particles was determined to be 5 nm on average, which was also confirmed by transmission electron microscopy (TEM) measurements (Figure S9 in the Supporting Information).[36]

Formation of metallic Ni particles has been previously reported during the preparation of powdered Ni catalysts from nickel-ethylenediamine precursors by calcination in an inert atmosphere.[25−28] This phase formation has been assigned to the generation of H_2 as a decomposition product of ethylenediamine. Similarly, other chelating agents have been studied that yield nickel nanoparticles since the decomposition mechanism of the chelating ligand is similar.[37] In this work, we demonstrate that this method yields small metallic particles also in the preparation of industrial-like catalysts based on millimeter-sized bodies.

In addition to this, after calcination, the pellet was observed to be entirely black suggestive of the presence of carbon on the catalyst body. This was confirmed by ex situ energy-dispersive X-ray (EDX) analysis (Figure S9 in the Supporting Information). The presence of carbon on this type of catalyst originates from the incomplete decomposition of the ethylenediamine ligand under an inert atmosphere because of the low amount of oxidizing agent (nitrates from the nickel precursor).[28,29] Most likely, this carbon then surrounded the nickel particles preventing their oxidation to NiO. Therefore, to obtain a usable catalyst containing Ni, the pellets must be further activated by a reduction or calcination (in air) treatment step to remove these carbonaceous compounds. This additional activation step can also induce a change in the Ni macrodistribution or morphology.

The various YZ distribution maps of the $[Ni(en)_3](NO_3)_2$ precursor recorded during calcination are presented in Figure 6 and represent the interior of the γ-Al_2O_3 catalyst body. As expected, these maps also show the breakdown of the complex as the temperature was increased during calcination. The YZ map at 25 °C confirms the $[Ni(en)_3](NO_3)_2$ crystalline egg-shell distribution throughout the whole pellet indicated by the YT map (Figure 4d). Interestingly, the distribution was not completely symmetrical at 25 °C as concluded from the red-coded regions only present on one side of the catalyst body. These irregularities may occur for several reasons, such as inhomogeneities in the support structure or manipulation of the catalyst during its preparation.[17,24] The YZ maps indicate that the precursor starts decomposing at around 70 °C, and by 190 °C, it has decomposed into a noncrystalline phase. The complex breakdown appears to occur at a much lower temperature than observed in some previous studies performed by Negrier et al.[29] who reported, from mass spectrometry (MS), that the decomposition of $[Ni(en)_3](NO_3)_2/\gamma$-$Al_2O_3$ under argon takes place at 350 °C. This temperature difference suggests that even though the $[Ni(en)_3](NO_3)_2$ precursor loses its crystallinity at low temperatures, possibly because of melting or amorphization, the decomposition products are not released until higher temperatures. The YZ maps also demonstrate that the decomposition actually takes place unevenly over the pellet occurring first in the core and then spreading toward the edges.

In summary, the calcination under N_2 of a $[Ni(en)_3](NO_3)_2/\gamma$-$Al_2O_3$ pellet leads to approximately 20% of Ni as 5 nm metallic Ni crystallites. The precursor salt, which appears in an egg-shell distribution before calcination, decomposes at 190 °C; this Ni profile is retained after calcination in the form of metallic Ni particles (at around 400 °C) protected with a carbon layer.

2. TEDDI during the Calcination of the $[Ni(en)(H_2O)_4]Cl_2/\gamma$-$Al_2O_3$ Pellet. Figure 7 shows the YT maps of the Ni distribution (both fluorescence and diffraction) constructed from various peaks observed in the energy-dispersive spectra. Prior to calcination, the $[Ni(en)(H_2O)_4]Cl_2/\gamma$-$Al_2O_3$ showed no Ni-related crystalline peaks, while the Ni fluorescence YT map revealed an even distribution of Ni throughout the body of the pellet as illustrated in Figure 7a. Additionally, UV−vis microspectroscopy confirmed this rather homogeneous distribution (Figure S10 in the Supporting Information).

Figure 7a illustrates that, as the sample was heated, an increase in the Ni fluorescence intensity occurred with temperature. This can be accounted for by changes in the density of the sample as the precursor decomposed as explained in

(36) Krawitz, A. D. In *Introduction to Diffraction in Materials Science and Engineering*; John Wiley & Sons: New York, 2001.
(37) Afanasiev, P.; Chouzier, S.; Czeri, T.; Pilet, G.; Pichon, C.; Roy, M.; Vrinat, M. *Inorg. Chem.* **2008**, *47*, 2303–2311.

Materials and Methods. Still, this map indicates a rather uniform distribution of Ni along the *y* direction of the catalyst body regardless of its molecular structure.

Interestingly, and unlike the $[Ni(en)_3](NO_3)_2/\gamma\text{-}Al_2O_3$ pellet, the calcination of the $[Ni(en)(H_2O)_4]Cl_2/\gamma\text{-}Al_2O_3$ pellet led to the formation of two intermediate crystalline phases before the formation of metallic Ni as illustrated in Figure 7b−7d. The spectra measured at the edge of the pellet during the calcination can be found in the Supporting Information (Figure S12). Several diffraction peaks were detected between 180 and 270 °C at 30.9, 33.3, 34.3, 36.9, 40.5, 53.5, 44.3, and 46.1 keV with the most intense at 36.9 and 40.5 keV. Since these peaks could not be assigned to a particular phase, we propose that a restructuring of the Ni species on the alumina surface is responsible for the changes in the energy-dispersive spectra, which yielded an ordered and unknown Ni phase. The essentially uniform blue color in the YT map of the peak at 36.9 keV (Figure 7b) indicates a rather uniform distribution along the catalyst body of this unknown Ni-containing crystalline phase. Moreover, this temperature range was in line with the release of NH_3 and H_2O followed with MS on a similar sample (3 wt % Ni as $[Ni(en)(H_2O)_4]Cl_2/\gamma\text{-}Al_2O_3$, Figure S11 in the Supporting Information).

Above 270 °C, the first Ni crystalline phase transforms into a second crystalline phase which is stable from 270 °C to approximately 430 °C. Several diffraction peaks were measured at 44.3, 46.8, 50.2, and 64.7 keV. These peaks were assigned, respectively, to the reflections (100), (002), (101), and (102) of hexagonal Ni_3C.[38] The low intensity of these peaks suggests that this phase is present as a maximum of 40% of the Ni species in the core of the pellet, while in the edges, less than 20% of Ni appears as Ni_3C (calculated on the basis of the relative intensities with respect to Ni° from reference patterns). Figure 7c shows the YT map of the peak at 50.2 keV and reveals that the stability of Ni_3C with temperature is dependent on its location in the catalyst body with a decomposition front moving toward the core with increasing temperature. At the edges of the pellet, Ni_3C decomposes almost immediately after being formed, while in the core, it is stable up to 430 °C and corresponds well with the known decomposition temperature of Ni_3C in an inert atmosphere, eq 1:[39]

$$Ni_3C \rightarrow 3Ni^o + C\ (s,\ amorphous) \qquad (1)$$

Finally, Figure 7d shows the formation of fcc metallic Ni, XY map of the (200) reflection. Similarly, as in the $[Ni(en)_3](NO_3)_2/\gamma\text{-}Al_2O_3$ pellet, the appearance of the reflections (111), (200), and (222) of fcc metallic Ni at high temperatures is observed. However, the $[Ni(en)(H_2O)_4]Cl_2/\gamma\text{-}Al_2O_3$ pellet shows very narrow and intense peaks, which suggests a large amount of Ni species converted into relatively large metallic Ni particles. This phase was initially observed at around 300 °C only at the edges of the catalyst and became uniform throughout the body at 435 °C. At 500 °C, the sample was held at temperature for 30 min during which time the concentration of Ni increased at the edges of the pellet indicating that sintering occurred.

Figure 8a shows the XY map of metallic Ni immediately after calcination and indicates a rather uniform distribution of metallic Ni (regions in green color), although there was some higher concentrations at the edge of the sample (yellow/orange regions).

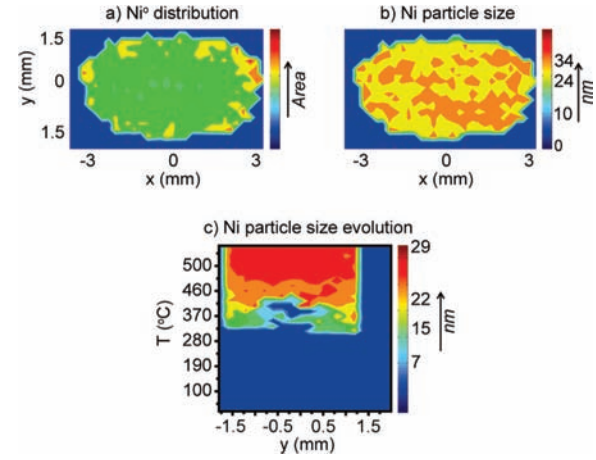

Figure 8. XY maps of (a) metallic Ni distribution in the $[Ni(en)(H_2O)_4]Cl_2/\gamma\text{-}Al_2O_3$ pellet after calcination at 500 °C, (b) particle size distribution of metallic Ni in the same slice of the pellet after calcination at 500 °C, and (c) evolution of metallic Ni crystallites as a function of the *y* direction of the catalyst body. The red color indicates regions of (a) higher concentration of metallic Ni or (b, c) larger particle size. The blue color indicates the absence of metallic Ni.

Using the full width at half-maximum (fwhm) of the metallic Ni (200) reflection and a Debye−Scherrer analysis, the particle size was estimated to be on average 24−34 nm as illustrated in Figure 8b. This value compared closely with that calculated from the ex situ XRD pattern measured on a crushed pellet (39 nm) (Figure S8 in the Supporting Information). Thus, relatively large nanoparticles of metallic Ni are formed when the Ni chloride precursor salt is used in equimolar concentrations of Ni and ethylenediamine.

Figure 8c illustrates the YT map of the evolution of metallic Ni crystallites with calcination temperature. The particle size growth was estimated assuming that at 500 °C the average particle size was 29 nm (average between 24 and 34 nm). The map indicates that metallic Ni particles appear readily at 300 °C, preferentially toward the edge of the pellet, while they are not observed in the core until 370 °C. Thus, between 370 and 430 °C, both Ni_3C and metallic Ni coexist in the pellet as can be deduced from Figure 7c and 7d. At around 435 °C, there is a uniform distribution of metallic Ni particles, which sinter to form larger particles at around 480 °C. Furthermore, unlike the $[Ni(en)_3](NO_3)_2/\gamma\text{-}Al_2O_3$ pellet, the $[Ni(en)(H_2O)_4]Cl_2/\gamma\text{-}Al_2O_3$ pellet was observed to be gray rather than black after calcination indicating the deposition of less carbon, which was confirmed ex situ using EDX analysis (Figure S9 in the Supporting Information).

To summarize, the use of $[Ni(en)(H_2O)_4]Cl_2$ as a precursor in the preparation of metallic Ni catalysts results in the formation of relatively large metallic Ni particles with a high degree of reduction when compared to $[Ni(en)_3](NO_3)_2$ (cf. 30−40 nm vs 5 nm). This makes the $[Ni(en)(H_2O)_4]Cl_2/\gamma\text{-}Al_2O_3$ catalyst less interesting for industrial applications. The formation of larger particles indicates that Ni-oxy-chloride species must become mobile during the calcination process. Moreover, the mobility of Ni species starts at around 180 °C, the temperature at which the first intermediate crystalline phase was detected, which suggests that this phase is implicit in the aggregation of the metal particles in this material. Moreover, large nanoparticles and a high heterogeneity in the particle size distribution of metallic Ni was confirmed by TEM measurements (Figure S9 in the Supporting Information). Even though TEDDI enables

(38) Nagakura, S. *J. Phys. Soc. Jpn.* **1958**, *13*, 1005–1014.
(39) Leng, Y.; Xie, L.; Liao, F.; Zheng, J.; Li, X. *Thermochim. Acta* **2008**, *473*, 14–18.

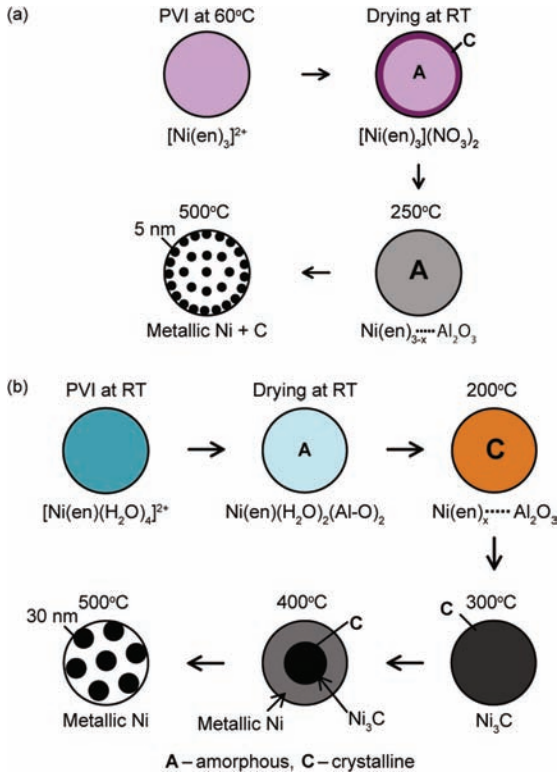

Figure 9. Phase transformation of (a) the $[Ni(en)_3](NO_3)_2/\gamma\text{-}Al_2O_3$ pellet and (b) the $[Ni(en)(H_2O)_4]Cl_2/\gamma\text{-}Al_2O_3$ pellet during catalyst preparation from pore volume impregnation (PVI) up to calcination at 500 °C in a N_2 gas atmosphere. The different colors represent the different phases present. After calcination at 500 °C, the particle size of metallic Ni is also indicated.

the visualization of the structural changes of Ni during the calcination process in a space-resolved manner, the mechanism by which large metallic Ni particles formed could not be deduced. With the knowledge gained by the TEDDI technique, a schematic of the preparation of metallic Ni catalyst bodies when the precursor salts $[Ni(en)(H_2O)_4]Cl_2$ and $[Ni(en)_3](NO_3)_2$ are used can be proposed as illustrated in Figure 9.

As illustrated in Figure 9a, pore volume impregnation of $[Ni(en)_3](NO_3)_2$ on $\gamma\text{-}Al_2O_3$ pellets yields a uniform profile of this Ni^{2+} complex along the catalyst body before drying. Drying at 20 °C induces the crystallization of large $[Ni(en)_3](NO_3)_2$ particles toward the outer rim of the catalyst bodies as inferred from the sharp diffraction peaks measured at low temperatures. During the calcination of this sample, the precursor $[Ni(en)_3](NO_3)_2$ decomposes at 190 °C forming an amorphous intermediate phase which remains in an egg-shell profile. Above 385 °C, small metallic Ni crystallites of around 5 nm size are formed (~20% of the Ni present), in the same egg-shell distribution, covered by carbonaceous species.

On the other hand, pore volume impregnation of $[Ni(en)(H_2O)_4]Cl_2$ yields a uniform macrodistribution of Ni before drying that remains unchanged during the subsequent preparation steps. Drying at 20 °C creates ligand-exchange reactions of the precursor complex with the hydroxylated surface of the $\gamma\text{-}Al_2O_3$ support forming $[Ni(en)(H_2O)_2(Al\text{-}O)_2]$ species. At 180 °C, the precursor complex undergoes decomposition as well as restructuring on the $\gamma\text{-}Al_2O_3$ surface and transforms into an intermediate crystalline phase, which is stable up to 270 °C. At this temperature, Ni restructures again partly forming Ni_3C species, and its stability depends on the location within the catalyst bodies. In this way, Ni_3C at the outer rim of the catalyst body decomposes readily forming metallic Ni at around 300 °C, while at the edges, it is stable up to 430 °C. This preparation method yields a large amount of Ni species converted into metallic Ni particles of sizes around 30−40 nm, which are less desired for catalytic applications because of their low activity.

Conclusions

TEDDI has been successfully employed for the first time to study the process of calcination of a heterogeneous catalyst; in particular, the genesis of the active structure in a catalyst body has been monitored. During this study, three types of data collections were performed including the standard 2D XY cross sections and, for the first time, time-resolved 1D Y scan-lines (which can also be considered as 2D scans with time as the extra dimension) and 2D YZ cross sections (3D scans: $y-z-$time scans). Thus, detailed insight into the changes in the structural composition at the macroscopic level in a noninvasive manner could be obtained. Most importantly, it was demonstrated that the formation of an active component is a multistep evolution process and that this process shows significant spatial variation. Since a major asset of the TEDDI technique is the simultaneous acquisition of both X-ray diffraction and fluorescence signals, it was possible to link the observations concerning the crystallinity of the sample and the less-ordered phases and how these evolved during calcination. Although the aim of this work was to demonstrate the applicability of TEDDI as a noninvasive tool to reveal insight into microstructure changes of a heterogeneous catalyst during heating in the presence of gases, the scope of such work could easily be extended into other fields of research. For example, insight into the stability and behavior of heterogeneous materials under different conditions of temperature and pressure and in different ambients (oxidizing, corrosive, or inert) are of prime importance in the fields of material science, chemistry, and geology as well as in a broad range of applications from medical to civil engineering or chemical industry.

Acknowledgment. B. M. W. and K. P. J. acknowledge financial support by ACTS-ASPECT. A. M. B. thanks NWO−CW for a VENI grant. P. B. and S. D. M. J. thank EPSRC for a portfolio grant. The authors also acknowledge EPSRC/CCLRC for beamtime on station 16.4 and Dave Taylor for technical assistance. The authors thank Taha Sochi at UCL for the development of the software used to analyze the data and Cor van der Spek at UU for TEM measurements.

Supporting Information Available: Details on the data processing and further characterization of the samples under study. This material is available free of charge via the Internet at http://pubs.acs.org.

JA907329J